Faculty Scholarship

2017

Diffuse Ionized Gas In The Milky Way Disk

Matteo Luisi

L. D. Anderson

Dana S. Balser

Trey V. Wenger

T. M. Bania

Follow this and additional works at: https://researchrepository.wvu.edu/faculty_publications

DIFFUSE IONIZED GAS IN THE MILKY WAY DISK

Matteo Luisi,[1, 2] L. D. Anderson,[1, 2, 3] Dana S. Balser,[4] Trey V. Wenger,[4, 5] and T. M. Bania[6]

[1]*Department of Physics and Astronomy, West Virginia University, Morgantown WV 26506, USA*

[2]*Center for Gravitational Waves and Cosmology, West Virginia University, Chestnut Ridge Research Building, Morgantown WV 26505, USA*

[3]*Adjunct Astronomer at the Green Bank Observatory, P.O. Box 2, Green Bank WV 24944, USA*

[4]*National Radio Astronomy Observatory, 520 Edgemont Road, Charlottesville VA 22903-2475, USA*

[5]*Astronomy Department, University of Virginia, P.O. Box 400325, Charlottesville, VA 22904-4325, USA*

[6]*Institute for Astrophysical Research, Department of Astronomy, Boston University, 725 Commonwealth Ave., Boston MA 02215, USA*

ABSTRACT

We analyze the diffuse ionized gas (DIG) in the first Galactic quadrant from $\ell = 18°$ to $40°$ using radio recombination line (RRL) data from the Green Bank Telescope. These data allow us to distinguish DIG emission from H II region emission and thus study the diffuse gas essentially unaffected by confusion from discrete sources. We find that the DIG has two dominant velocity components, one centered around 100 km s^{-1} associated with the luminous H II region W43, and the other centered around 45 km s^{-1} not associated with any large H II region. Our analysis suggests that the two velocity components near W43 may be caused by non-circular streaming motions originating near the end of the Galactic bar. At lower Galactic longitudes, the two velocities may instead arise from gas at two distinct distances from the Sun, with the most likely distances being $\sim$6 kpc for the 100 km s^{-1} component and $\sim$12 kpc for the 45 km s^{-1} component. We show that the intensity of diffuse *Spitzer* GLIMPSE $8.0\,\mu$m emission caused by excitation of polyaromatic hydrocarbons (PAHs) is correlated with both the locations of discrete H II regions and the intensity of the RRL emission from the DIG. This implies that the soft ultra-violet photons responsible for creating the infrared emission have a similar origin as the harder ultra-violet photons required for the RRL emission. The $8.0\,\mu$m emission increases with RRL intensity but flattens out for directions with the most intense RRL emission, suggesting that PAHs are partially destroyed by the energetic radiation field at these locations.

Keywords: H II regions – ISM: abundances – ISM: kinematics and dynamics – ISM: structure – radio lines: ISM

1. INTRODUCTION

First proposed by Hoyle & Ellis (1963), the warm interstellar medium (WIM) is a widespread component of the interstellar medium (ISM) with density $\sim 0.1\,\mathrm{cm^{-3}}$ and temperatures from 6000 to 10000 K (see Haffner et al. 2009, and references therein). At the upper end of this temperature range, the WIM is nearly fully ionized, with a hydrogen ionization ratio $n(\mathrm{H^+})/n(\mathrm{H^0}) \geq 13$ (Reynolds et al. 1998). Thus, the WIM is also known as the "Diffuse Ionized Gas" (DIG). Despite its low density, $\sim$80–90% of the total free-free emission in our Galaxy is thought to come from the DIG.

Though the exact mechanisms are still unknown, it is believed that the DIG maintains its ionization from O-type stars, whose UV radiation leaks out of the H II regions surrounding them and into the ISM (Reynolds 1984; Ferguson et al. 1996; Zurita et al. 2002). Murray & Rahman (2010) confirmed that a large number of ionizing photons are leaking from H II regions. Anderson et al. (2015) derived an ionizing radiation leaking fraction of $\sim$25% for the bubble H II region RCW 120 using Hα data at 656 nm. They also showed that the photodissociation region (PDR) surrounding the H II region has distinct "holes" through which photons can escape into the ISM. This suggests that PDRs are generally not homogeneous. Recently, we showed that the non-uniform PDR surrounding the compact H II region NGC 7538 allows radiation to escape preferentially along a single direction (Luisi et al. 2016). We calculated a leaking fraction $f_R = 15 \pm 5\%$ of the radio continuum emission. This leaking emission appears spatially confined within an additional, more distant PDR boundary around NGC 7538 and thus seems to only affect the local ambient medium. Results suggest, however, that giant H II regions such as W43 may have a much larger effect in maintaining the ionization of the DIG and despite their small numbers may be the dominant source of ionizing radiation in the ISM (see Zurita et al. 2000).

Together with H II regions and PDRs, the DIG is a major source of radio recombination line (RRL) emission. Consequently, RRL observations have been used to map its spatial and velocity distribution. Compared to studies of optical emission lines, specifically Hα (e.g., the WHAM survey, Haffner et al. 1999), RRL observations have the advantage of essentially being free from extinction due to interstellar dust. Their disadvantage is reduced sensitivity, restricting RRL detections to gas with higher emission measure than that traced by Hα. The fully-sampled 1.4 GHz RRL survey of Alves et al. (2010, 2012, 2015) mapped the plane of the Galaxy at a spatial resolution of 14′.4. They were, however, unable to distinguish the contributions from discrete H II regions and the DIG for most sight lines. The observing method of the fully-sampled SIGGMA RRL survey (Liu et al. 2013) partially filters out the emission from the DIG. Finally, Roshi & Anantharamaiah (2001) observed the Galactic plane in RRLs near 327 MHz from $-28° < \ell < 89°$. Despite the low resolution of $\sim$2°, they obtain an upper limit of 12,000 K for the electron temperature of the gas and suggest that the emission originates from low-density ionized gas forming H II region envelopes.

With the emergence of high-sensitivity RRL surveys, the DIG has been serendipitously detected in observations of discrete H II regions (see Anderson et al. 2015, and references therein). In the Green Bank Telescope H II Region Discovery Survey (GBT HRDS, see Bania et al. 2010; Anderson et al. 2011) we identified multiple RRL velocity components in $\sim$30% of all observed targets. This fraction is too large to be caused by multiple discrete H II regions along the line of sight (see Anderson et al. 2015). We thus infer that the RRL emission at these locations is usually composed of emission from a discrete source and emission from the DIG (Anderson et al. 2015).

Here, we use data from past observations (Anderson et al. 2011; Anderson et al. 2015) and previously unpublished data for directions either known to be devoid of discrete H II regions, or in directions where the H II region emission can be distinguished from that of the DIG (see §2 for details on how we distinguish between these two components). This gives us an irregularly-spaced grid of pointings, for which we can extract the intensity and velocity of only the DIG. The advantage of our strategy is that the beam size is relatively small (82″) compared with typical spacings between discrete H II regions so the emission at each pointing is not contaminated with H II region emission. The disadvantage of course is that the (ℓ, b)-space is not fully sampled. By distinguishing the emission from discrete H II regions and the DIG, our data allows us to essentially filter out H II region emission entirely and map only the diffuse component. This gives us an advantage over previous RRL surveys (Liu et al. 2013; Alves et al. 2015) as these are at least partially contaminated by H II region emission. With this analysis we are able to investigate the relationship between discrete H II regions and the diffuse gas, and test our hypothesis that large H II regions are dominant in maintaining the ionization of the DIG (Zurita et al. 2000; Luisi et al. 2016).

2. DIG RRL EMISSION

Our RRL emission data were taken with the Auto-Correlation Spectrometer (ACS) on the National Radio Astronomy Observatory Green Bank Telescope (GBT). We observed a total of 254 directions between $\ell = 18°$ and $40°$ and $|b| < 1°$ which yielded 379 sets of line parameters for the DIG. Our data come from two previously published sources, Anderson et al. (2011) and Anderson et al. (2015), and one previously unpublished source (see below). Anderson et al. (2011) contains directions coincident with H II regions, as defined by $8\,\mu m$ Spitzer GLIMPSE emission, for which the diffuse gas velocity can be distinguished from the H II region velocity (these data include 98 pointings with 116 sets of diffuse line parameters). The process of distinguishing the diffuse gas velocities from H II region velocities is described in Anderson et al. (2015). We use previous GBT observations, analyze the derived electron temperature for each velocity component, and search for the molecular emission or carbon recombination lines associated with one RRL component. Sight lines that that do not pass within the $8\,\mu m$-defined H II region PDR are always considered "diffuse." Anderson et al. (2015) also includes such directions devoid of discrete H II regions which allows us to directly sample the DIG without confusion (135 pointings; 237 sets of line parameters).

We also incorporate observations taken near the giant H II region W43 (21 pointings; 26 sets of diffuse line parameters) which we have not published previously. Here, we use our HRDS data to distinguish the diffuse gas velocity from the H II region velocity. If the observed direction is spatially coincident with a known H II region, we assume that the velocity component closest to the H II region velocity is due to the H II region itself. We summarize these data in Table 1, which lists the source, the Galactic longitude and latitude, the hydrogen line intensity, the FWHM line width, the local standard of rest (LSR) velocity, and the rms noise in the spectrum, including all corresponding 1σ uncertainties of the Gaussian fits. For directions with multiple velocity components detected along the line of sight, the source names are given additional letters, "a," "b," or "c," in order of decreasing peak line intensity. Velocity components that are due to discrete H II regions are marked with an asterisk in the table and are not used for our data analysis. For each observed direction, we simultaneously measured 7 Hnα RRL transitions in the 9 GHz band, H87α to H93α, using our standard techniques (Bania et al. 2010; Balser et al. 2011; Anderson et al. 2011), and averaged all spectra together to increase the signal-to-noise
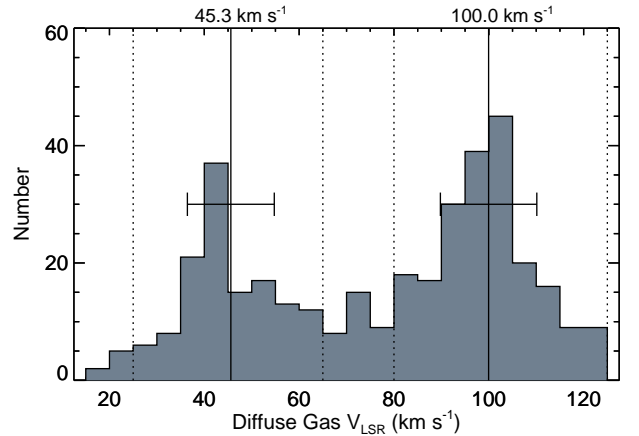

Figure 1. Velocity distribution of the DIG. The LSR velocities are derived from Gaussian fits to our RRL data. The dotted lines are defined by eye and show the velocity ranges that contain the majority of the diffuse gas velocities: the $45\ \mathrm{km\,s^{-1}}$ component at $25-65\ \mathrm{km\,s^{-1}}$ and the $100\ \mathrm{km\,s^{-1}}$ component at $80-125\ \mathrm{km\,s^{-1}}$. The solid lines and error bars indicate the mean velocities within these ranges and their standard deviations.

ratio using TMBIDL[1] (Bania et al. 2014). We assume that the brightest line emission from the DIG is due to hydrogen and fit a Gaussian model to each line profile. We use the line intensities, full width at half maximum (FWHM) values, and LSR velocities derived from the Gaussian fits for all further analysis.

3. DISCUSSION

3.1. The Galactic Location of the DIG

Over the longitude range considered here, the DIG emission is concentrated near two velocities, $45\ \mathrm{km\,s^{-1}}$ and $100\ \mathrm{km\,s^{-1}}$ (Figure 1). This suggests that within our observed Galactic longitude range the DIG itself is located at two distinct distances, assuming that the diffuse gas in each velocity range can be assigned a single distance. We summarize the DIG emission properties in Table 2.

Just as for the discrete sources, however, this diffuse gas also suffers from the kinematic distance ambiguity (KDA). Unfortunately, we cannot use the H I emission/absorption (H I E/A) method (Kuchar & Bania 1994; Kolpak et al. 2003; Anderson et al. 2012) for the DIG, both because it is faint and also because of the difficulty in finding a suitable "off" position. Only massive stars can produce ionizing photons energetic enough to create and maintain the DIG (e.g., Reynolds 1984). We can therefore potentially determine the kinematic dis-

---

[1] V7.1, see https://github.com/tvwenger/tmbidl.git.

LUISI ET AL.

Table 1. RRL Emission Near W43

Source	ℓ	b	T_L	σT_L	ΔV	$\sigma \Delta V$	V_{LSR}	σV_{LSR}	rms	Note[a]
	(degree)	(degree)	(mK)	(mK)	$(\,\mathrm{km\,s^{-1}})$	$(\,\mathrm{km\,s^{-1}})$	$(\,\mathrm{km\,s^{-1}})$	$(\,\mathrm{km\,s^{-1}})$	(mK)	
G030.400+0.180	30.400	+0.180	8.2	0.1	58.7	1.5	88.1	0.5	0.7	
G030.570−0.230	30.570	−0.230	38.8	0.3	19.3	0.2	88.1	0.1	0.4	*
G030.570+0.090a	30.570	+0.090	27.6	0.3	23.2	0.3	42.4	0.1	1.7	
G030.570+0.090b	30.570	+0.090	22.0	0.3	24.9	0.4	104.9	0.2	1.7	
G030.650−0.150a	30.650	−0.150	53.8	0.2	22.0	0.1	96.0	0.1	0.5	
G030.650−0.150b	30.650	−0.150	24.1	0.2	18.4	0.2	119.3	0.1	0.5	
G030.740−0.060	30.740	−0.060	617.6	1.5	24.2	0.1	90.7	0.1	2.1	*
G030.740+0.010	30.740	+0.010	612.5	0.7	29.5	0.1	91.1	0.1	2.3	*
G030.740+0.100a	30.740	+0.100	34.8	0.3	21.5	0.2	120.9	0.1	1.6	
G030.740+0.100b	30.740	+0.100	24.3	0.3	19.8	0.3	88.0	0.1	1.6	*
G030.740+0.100c	30.740	+0.100	9.9	0.3	20.5	0.7	39.9	0.3	1.6	
G030.740+0.180a	30.740	+0.180	12.8	0.2	46.7	1.1	96.6	0.4	1.5	*
G030.740+0.180b	30.740	+0.180	12.5	0.3	21.6	0.7	39.5	0.3	1.5	
G030.740+0.260a	30.740	+0.260	50.3	0.4	20.7	0.2	100.5	0.1	1.3	*
G030.740+0.260b	30.740	+0.260	13.1	0.4	19.7	0.7	37.0	0.3	1.3	
G030.740+0.280a	30.740	+0.280	64.2	0.4	19.7	0.1	100.8	0.1	1.2	*
G030.740+0.280b	30.740	+0.280	9.9	0.4	20.3	0.8	37.2	0.4	1.2	
G030.740+0.300a	30.740	+0.300	34.0	0.3	16.9	0.2	102.4	0.1	1.3	*
G030.740+0.300b	30.740	+0.300	11.3	0.2	23.5	1.1	79.0	0.5	1.3	
G030.740+0.300c	30.740	+0.300	7.6	0.2	22.3	0.8	36.7	0.3	1.3	
G030.740+0.350a	30.740	+0.350	15.8	0.3	14.7	0.5	78.2	0.2	1.2	
G030.740+0.350b	30.740	+0.350	15.7	0.3	21.6	0.6	102.3	0.2	1.2	
G030.740+0.350c	30.740	+0.350	3.6	0.2	35.4	3.7	39.5	1.2	1.2	
G030.740+0.430	30.740	+0.430	8.8	0.3	28.0	1.0	98.8	0.4	1.7	
G030.740+0.510a	30.740	+0.510	8.2	0.2	34.8	0.8	92.1	0.3	1.2	
G030.740+0.510b	30.740	+0.510	5.7	0.3	10.7	0.6	18.9	0.3	1.2	
G030.780−0.020	30.780	−0.020	2179.2	2.6	31.4	0.1	91.7	0.1	4.8	*
G030.780+0.010	30.780	+0.010	227.1	0.4	31.4	0.1	92.6	0.1	2.2	*
G030.820−0.060	30.820	−0.060	280.0	0.4	29.0	0.1	106.3	0.1	1.8	*
G030.820+0.180a	30.820	+0.180	14.0	0.2	18.5	0.3	36.4	0.1	0.8	
G030.820+0.180b	30.820	+0.180	11.3	0.1	38.7	0.5	99.6	0.2	0.8	*
G030.900−0.060a	30.900	−0.060	33.1	1.7	18.3	0.4	107.3	0.4	1.2	
G030.900−0.060b	30.900	−0.060	14.5	0.8	23.5	1.9	90.0	1.3	1.2	
G030.900−0.060c	30.900	−0.060	4.6	0.2	31.2	1.8	45.7	0.7	1.2	
G030.900+0.340a	30.900	+0.340	7.3	0.1	37.3	0.7	103.4	0.3	0.8	
G030.900+0.340b	30.900	+0.340	2.8	0.1	28.6	1.7	38.4	0.7	0.8	
G031.070−0.150a	31.070	−0.150	13.8	0.2	28.6	0.4	99.0	0.2	0.9	
G031.070−0.150b	31.070	−0.150	4.3	0.2	25.8	1.4	26.2	0.6	0.9	

[a] RRL components associated with discrete H II regions are marked with an asterisk (*, see text).

Table 2. DIG Parameters

Velocity range	45 km s^{-1}	100 km s^{-1}
Number of RRL components (total)	128	211
Number of RRL components (on)[a]	33	63
Number of RRL components (off)	95	148
Mean velocity (km s^{-1})	45.3	100.0
Median velocity (km s^{-1})	43.0	99.4
Std. Dev. velocity (km s^{-1})	9.2	10.1
Mean T_A (mK)	12.5	16.8
Median T_A (mK)	9.8	13.6
Std. Dev. T_A (mK)	9.6	11.2
Near distance (kpc)	1.7 − 3.7	4.4 − 7.2
Far distance (kpc)	10.6 − 12.7	7.2 − 10.0
Assumed distance (kpc)	∼12	∼6
Total integrated flux (Jy)	172.8	246.0
Total integrated flux (Jy)[b]	118.3	220.4

[a] "on" and "off" correspond to directions coincident with H II regions (on), and directions devoid of discrete H II regions (off).

[b] From Alves et al. (2015).

tance for the diffuse gas by associating it with massive star formation tracers that have their KDA resolved: massive H II regions, molecular gas, and cold H I.

Below, we attempt to find the distance to the two observed velocity components of the DIG by resolving their KDA. In §3.1.1 and §3.1.2 we assume that each velocity component can be assigned a single distance from the Sun. In §3.1.3 we explore the possibility of the two observed velocity components being due to interacting gas clouds at the same distance from the Sun.

3.1.1. *The 45 km s^{-1} Gas Component*

The KDA leads to two possible distance ranges for each velocity range. The 45 km s^{-1} gas could be at either $1.7 − 3.7$ kpc or $10.6 − 12.7$ kpc, if we assume $(\ell, b) = (30°, 0°)$, and use the Reid et al. (2014) rotation curve (see Table 2).

Assuming that the DIG is maintained by massive stars, we can use the ionization rate of H II regions as a tracer to determine the distance to the DIG. In the range $\ell = 18°$ to $40°$, there are 205 H II regions with velocities between 25 and 65 km s^{-1}, and 127 of these have kinematic distance ambiguity resolutions (KDARs; Anderson et al. 2014, The WISE Catalog of Galactic

H II Regions, Version 1.4[2]). The total radio flux density of the 94 regions at the far kinematic distance is 10.84 Jy, whereas the total flux density of the 33 regions at the near kinematic distance is only 1.09 Jy. We estimate the ionization rate for each region using our HRDS data (Rubin 1968; Anderson 2010) by

$$N_{\mathrm{ly}} \approx 4.76 \times 10^{48} \left(\frac{S_\nu}{\mathrm{Jy}}\right) \left(\frac{T_e}{\mathrm{K}}\right)^{-0.45} \left(\frac{\nu}{\mathrm{GHz}}\right)^{0.1} \left(\frac{d}{\mathrm{kpc}}\right)^2, \quad (1)$$

where N_{ly} is the ionization rate, the number of emitted Lyman Continuum ionizing photons per second, S_ν is the radio flux density of the H II region, T_e is the electron temperature, $\nu = 1.4$ GHz is the observed frequency (see Anderson et al. 2011), and d is the distance to the region. We assume a constant $T_e = 10^4$ K and sum the contribution for each individual region to find the total N_{ly} for H II regions at the far and near kinematic distance. This estimate yields $N_{\mathrm{ly}} = 1.06 \times 10^{50}$ s^{-1} for the far distance and only $N_{\mathrm{ly}} = 5.80 \times 10^{47}$ s^{-1} for the near distance. This suggests that most of the DIG near 45 km s^{-1} is also at the far kinematic distance.

There is also over twice as much total CO gas at the far kinematic distance for clouds in the velocity range 25 to 65 km s^{-1} compared to the near distance. The average near GRS cloud CO luminosity from Roman-Duval et al. (2009) in units of 10^4 K km s^{-1} pc^{-2} is 0.23 with a standard deviation of 0.31, while it is 1.4 with a standard deviation of 1.7 for the far GRS clouds. The total CO luminosity for the near clouds is 3.4×10^5 K km s^{-1} pc^{-2}, while it is 8.0×10^5 K km s^{-1} pc^{-2} for the far GRS clouds. This again supports the 45 km s^{-1} DIG being at the far kinematic distance, if it is indeed associated with the molecular gas traced by CO emission that will continue to form massive stars.

Finally, we investigate the location of the cold H I gas using the H I E/A method. Only cold H I foreground to a radio continuum source will cause H I absorption, assuming that H I self-absorption is negligible. The H I spectrum toward an extragalactic radio continuum source can show absorption for all H I along the line of sight, while for Galactic sources the H I spectrum can only show absorption up to the source velocity. Comparing the H I spectra toward nearby extragalactic and Galactic H II region pairs can therefore tell us about the H I distribution. If cold H I gas is foreground to the H II region, we expect to see absorption in both spectra. Cold H I beyond the H II region, however, will only show absorption in the spectrum toward the extragalactic source.
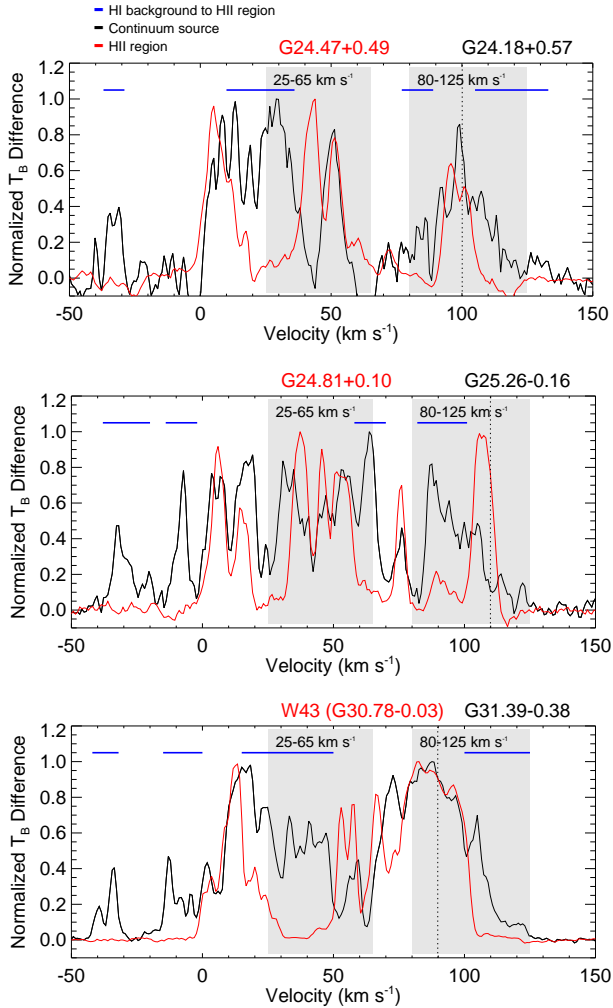
---

[2] see http://astro.phys.wvu.edu/wise/

Figure 2. H I absorption spectra towards H II regions and extragalactic radio sources to investigate the KDAR of the DIG. The difference in VGPS main beam temperature, normalized by the maximum observed temperature, is shown between on- and off-target directions for H II regions (red curves) and extragalactic radio continuum sources (black curves). The top panel shows the H II region G24.47+0.49 and the extragalactic source G24.18+0.57, the middle panel shows G24.81+0.10 and the extragalactic source G25.26−0.16, and the bottom panel shows W43 at $(\ell, b) \simeq (30.8°, 0.0°)$ and the extragalactic source G31.39−0.38. The H II region RRL velocities are shown with dotted lines. Shaded regions indicate the two dominant velocity ranges of the DIG emission. Continuum source spectra showing absorption not present in the H II region spectra should be background to the H II region; these velocities are marked with horizontal blue lines at the top of each plot. This analysis implies that most of the H I below 50 km s^{-1} near W43 is at the far kinematic distance.

Here we use the Very Large Array Galactic Plane Survey (VGPS; see Stil et al. 2006) spectral line data to compare the H I E/A spectrum for three H II regions (G24.47+0.49, G24.81+0.10, and W43) with velocities near 100 km s^{-1}. All three have nearby (within ∼40′) extragalactic radio continuum sources. Figure 2 shows the difference between on- and off-target directions for the H II regions and extragalactic radio sources, where the on- and off-positions are separated by 6′. The H II regions are located either foreground or background to the 45 km s^{-1} gas, depending on their KDARs. As a result, H I gas at velocities showing extragalactic absorption which is not present in the H II region spectra should be background to the H II region. This analysis implies that most of the H I below 50 km s^{-1} near W43 is at the far kinematic distance. The first H I spectrum pair (G24.47+0.49) extracted near $\ell = 24°$ shows partial absorption near 45 km s^{-1} that is inconsistent with the absorption features seen in the second pair near $\ell = 24°$ (G24.81+0.10). Therefore, we can not assign a single distance to the H I near the $\ell = 24°$ region. These results are somewhat ambiguous, however, since the separation between the line of sight towards the H II regions and the extragalactic continuum sources are probing different H I volumes.

Since both the total H II region ionization rate and the fraction of molecular gas are greater at the far distance, we favor the conclusion that most of the 45 km s^{-1} diffuse gas is at its far kinematic distance of ∼12 kpc as well. This is a simplified assumption and does not take into account the existence of additional gas at the other distance.

3.1.2. The 100 km s^{-1} Gas Component

The possible distance range for the 100 km s^{-1} gas is $4.4 − 10.0$ kpc for $(\ell, b) = (30°, 0°)$. Because the molecular gas and massive star formation for the $80 − 100$ km s^{-1} (ℓ, b, v) locus is associated with W43 (e.g., Nguyen Luong et al. 2011) at a distance of $5.49^{+0.39}_{-0.34}$ kpc (Zhang et al. 2014), we assume throughout the remainder of this paper that the 100 km s^{-1} DIG is at a distance of ∼6 kpc. Recently, Langer et al. (2017) observed the DIG along 18 lines of sight between $\ell = 30°$ and $32°$ using the [C II] 158 μm and [N II] 205 μm fine structure lines. They find a strong line component near ∼115 km s^{-1} and argue that this component is due to DIG emission associated with the inner edge of the Scutum spiral arm tangency at a distance of ∼7 kpc. Even if our assumption that the gas is at the distance of ∼6 kpc is poor, our conclusions below are largely unaffected.

3.1.3. *Interacting Gas Clouds?*

Our detection of the DIG in two separate velocity ranges suggests that each velocity range is primarily located at either its near or its far kinematic distance. If the two velocity components are indeed interacting, we would expect to observe an interaction signature between them. Such an interaction signature has been suggested by Beuther et al. (2012) for the $^{13}CO(2-1)$ emission near the W43 region, as well as for dense gas tracers like N_2H^+. In the Milky Way, however, this picture is further complicated by the vicinity of the 45 $km\,s^{-1}$ component to the Galactic bar and the Scutum arm. Using an extragalactic counterpart to the W43 region, Beuther et al. (2017) argue that gas buildup near the bar/spiral arm interface, where W43 is located, is likely due to crossings between different orbit families. They posit that the observed velocities in the bar/spiral arm interface of NGC 3627 are primarily due to interacting gas clouds.

If we assume that the observed velocities toward the $\ell \sim 30°$ region are due to interacting gas clouds at a single distance, we can use the method described by Beuther et al. (2017) to estimate the expected gas velocities observed along the line of sight and compare these with our observations. The simplest approximation assumes that the observed diffuse gas towards W43 is located at the tip of the Galactic bar, and that the two observed velocity signatures are due to the unperturbed, purely circular gas motion around the Galactic center and gas streaming motions along the bar, respectively. Using the Reid et al. (2014) rotation curve, we find a circular gas velocity, $V_C \sim 230$ $km\,s^{-1}$ for the observed diffuse gas towards W43. This corresponds to a velocity component along the line of sight of 91 $km\,s^{-1}$, almost identical to the observed velocity of 89.8 $km\,s^{-1}$ for W43 itself. The perturbed velocity component due to streaming motions can be described by determining the bar perturbation to the gravitational potential (see Sellwood & Sánchez 2010; Beuther et al. 2017). Since we only consider emission from the end of the bar, the radial streaming velocity component must go to zero, and the resultant azimuthal velocity component, v_ϕ^B, is

$$v_\phi^B \sim \left(1 - \frac{1 - q_\phi^2}{4q_\phi^2}\right) V_C, \qquad (2)$$

where q_ϕ is the axial ratio of the bar potential. We use $1 - q_\phi \simeq \frac{1}{3}(1 - q)$ from Binney & Tremaine (2008, p. 77), where $q = 0.3-0.4$ is the axial ratio of the density distribution for the Milky Way bar (Bissantz & Gerhard 2002). We adopt $q = 0.35 \pm 0.05$ and find that $v_\phi^B = 0.84 \pm 0.02\,V_C$. Observed along the line of sight, this
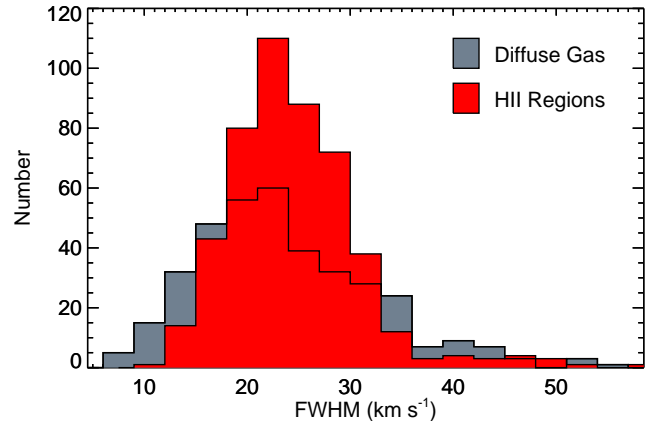

Figure 3. Distribution of FWHM line widths of directions coincident with discrete H II regions and the DIG. There is no significant difference between the average line widths of H II regions and the DIG (see text), indicating that turbulence does not play a major role in altering the observed velocity of the diffuse gas.

corresponds to a velocity of 57 ± 4 $km\,s^{-1}$ which is near our observed 45 $km\,s^{-1}$ velocity component.

Although the above method describes the observed velocity components near $\ell \sim 30°$ fairly well, the assumption that the gas is located at the end of the Galactic bar breaks down when considering gas emission from the $\ell \sim 24°$ region further within the bar where we observed a similar velocity distribution. To describe the kinematics of the gas at this location, we must include radial streaming motions along the bar (Sellwood & Sánchez 2010; Beuther et al. 2017) which can be estimated by

$$v_r^B \sim \frac{2}{3}\left(1 - \frac{1 - q_\phi^2}{4q_\phi^2}\right) V_C. \qquad (3)$$

We repeat the analysis above for the $\ell \sim 24°$ region, and find an unperturbed velocity component along the line of sight of 96 $km\,s^{-1}$, and a perturbed velocity component of 7 ± 2 $km\,s^{-1}$. In theory, shocks and turbulence could increase the latter to match our observed 45 $km\,s^{-1}$ emission. While we can not quantify the amount of turbulence in the DIG directly, we can compare the observed hydrogen recombination line widths at the diffuse directions with the line widths of directions coincident with discrete H II regions. Assuming the same electron temperature, differences in line widths should trace the relative strength of turbulence between these directions. We find, however, no statistically significant difference of line widths between directions coincident with H II regions (FWHM = 24.5 ± 6.4 $km\,s^{-1}$) and our diffuse directions (FWHM = 23.7 ± 8.8 $km\,s^{-1}$). We show the corresponding FWHM line width distributions in Figure 3. This suggests that turbulence does not play a sig-

nificant role in altering the observed velocity of the gas. As a result, the large difference of the derived $7\,\mathrm{km\,s^{-1}}$ velocity component to our observed $45\,\mathrm{km\,s^{-1}}$ emission makes it doubtful whether interacting gas clouds at a single distance near $\ell \sim 24°$ could result in the observed velocity distribution.

Although the simple model discussed above suggests that interacting gas clouds can not account for our observed data, a more thorough numerical analysis would be required to confirm this result. Renaud et al. (2013, 2015) developed a hydrodynamical simulation of a Milky Way-like galaxy which includes star formation and stellar feedback through photoionization, radiative pressure and supernovae. They find that the leading edges of bars are favorable locations for converging gas flows and shocks. A similar model, focusing on bar kinematics in particular, may provide more insight towards the interaction processes near the bar-spiral arm interface.

3.2. *Intensity and Distribution of the DIG*

Our database of RRL parameters from the HRDS also allows us to investigate the spatial distribution of the DIG in the plane of the sky. Using our irregularly gridded data points, we examine the diffuse gas separately for the two velocities, $45\,\mathrm{km\,s^{-1}}$ and $100\,\mathrm{km\,s^{-1}}$. We create maps of the DIG in these two velocity ranges by interpolating the irregularly-spaced grid of 233 points to create pixels $6'$ square. We do this by first performing a Delauney triangulation (using the IDL program "qhull") and then create an (ℓ, b) map of the RRL intensity from the DIG using inverse distance weighting (using the IDL program "griddata"). This method has the advantage that the maximum and minimum values in the interpolated surface can only occur at sample points. We assume that the top and bottom edges of the map $(b = \pm 1°)$ have zero intensity to ensure that the emission is constrained in latitude. We show these images in Figure 4 for the two velocity ranges. We also show in Figure 4 the 1.4 GHz H I Parkes All-sky survey RRL map (Alves et al. 2015) averaged over the velocity ranges of the $45\,\mathrm{km\,s^{-1}}$ and $100\,\mathrm{km\,s^{-1}}$ components for comparison. The green circles in Figure 4 show the locations of discrete H II regions cataloged by Anderson et al. (2014, Version 1.4) that are within the velocity range of interest, while the gray crosses show locations where the DIG was detected within the velocity range.

Using the same data set of RRL parameters, we explore the velocity distribution of the DIG in more detail. We create a longitude-velocity diagram of the DIG by interpolating between our grid points (Figure 5, top panel), and assume that the velocity edges of the diagram (at $0\,\mathrm{km\,s^{-1}}$ and $130\,\mathrm{km\,s^{-1}}$) have zero intensity

so that the emission is constrained in velocity space. This assumption appears valid, since we did not detect any RRL components outside of this velocity range. In fact, our smallest and largest detected velocities at $18\,\mathrm{km\,s^{-1}}$ and $124\,\mathrm{km\,s^{-1}}$, respectively, are well within this range. For comparison, we also show a longitude-velocity diagram of $^{12}\mathrm{CO}$ used to trace molecular clouds (Figure 5, bottom panel; data from Dame et al. 1987).

3.2.1. *The $45\,\mathrm{km\,s^{-1}}$ Gas Component*

The pixel-by-pixel correlation of RRL intensity at $45\,\mathrm{km\,s^{-1}}$ between our maps and the Alves et al. (2015) data is poor (see Figure 6, top panel). Our emission towards W43 near $\ell \sim 30°$ and the $\ell \sim 24°$ region is disproportionately large in the $45\,\mathrm{km\,s^{-1}}$ map, whereas we do not see strong emission near the map edge at $\ell \sim 19°$. This may be due to interpolation errors between our sparse RRL pointings in this velocity and longitude range. Our low number of pointings may also be the cause of some of the more extended RRL emission between W43 and the $\ell \sim 24°$ complex that is less pronounced in the Alves et al. (2015) data. This makes it challenging to distinguish between interpolation errors and actual diffuse gas below the Parkes 1.4 GHz RRL survey's sensitivity threshold for the undersampled regions in our maps. Additionally, the beam size of $\sim 14'$ in the Alves et al. (2015) maps is too large to avoid H II regions at locations where their number density is high. Thus, most of their emission towards W43 and the $\ell \sim 24°$ region must be caused by discrete H II regions rather than the DIG. Overall, the total integrated intensity of our maps is 46% larger in the $45\,\mathrm{km\,s^{-1}}$ component compared with the Alves et al. (2015) data. This perhaps indicates that we are more sensitive to the diffuse gas.

3.2.2. *The $100\,\mathrm{km\,s^{-1}}$ Gas Component*

While the interpolated $45\,\mathrm{km\,s^{-1}}$ map shows poor agreement with the Alves et al. (2015) data, our $100\,\mathrm{km\,s^{-1}}$ map is strongly correlated with the 1.4 GHz RRL emission data (Figure 6, bottom panel). By-eye comparison of the two maps (Figure 4) indicates that we are more sensitive to the diffuse gas component, especially at lower Galactic longitudes. The total integrated intensity of our data is 10% larger in the $100\,\mathrm{km\,s^{-1}}$ component compared to Alves et al. (2015) (see Table 2). Figure 5 (top panel) shows that much of the $100\,\mathrm{km\,s^{-1}}$ emission from the DIG may be associated with the Scutum spiral arm. The higher velocities of the DIG compared to the Scutum arm may indicate that we are observing strong streaming motions in this direction (see Bania et al. 2012). Alternatively, the DIG may be located near the inner edge of the Scutum tangency
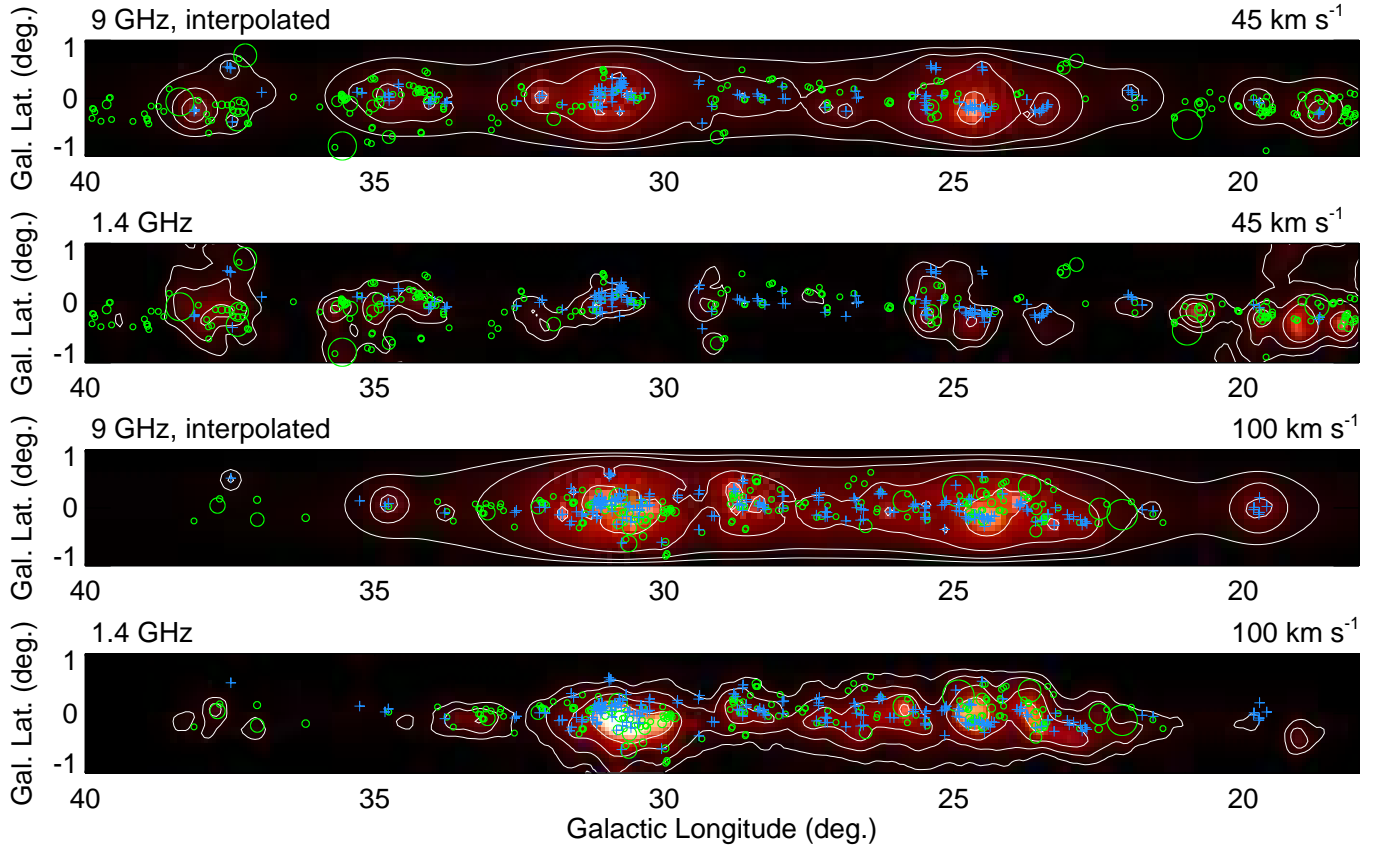
Figure 4. RRL emission over our observed longitude range. Top panel: Image of the diffuse gas emission for the 45 km s^{-1} velocity component. This image was made by interpolating our irregularly gridded 9 GHz RRL data. The color scale shows the emission ranging linearly from 0 to 30 mK, and the contours are at 2, 4, 8, and 16 mK. The locations of the diffuse emission in this velocity range are marked by blue crosses, and green circles mark H II regions from the velocity range indicated. The H II region circle sizes and locations are from Anderson et al. (2014), with a minimum circle size of 0.1° for better visibility. Second from top: Parkes 1.4 GHz RRL survey map, integrated for the 45 km s^{-1} velocity component (Alves et al. 2015). Unlike our interpolated image above, the 1.4 GHz data includes emission from discrete H II regions. The color scale shows the emission ranging linearly from 0 to 200 mK, and the contours are at 15, 30, 60, and 120 mK. Third from top: Same as top panel, but for the 100 km s^{-1} velocity component. Bottom panel: Parkes RRL survey map for the 100 km s^{-1} velocity component (scale and contours equivalent to second panel from top).

where it is falling into the arm's gravitational potential, as suggested by Langer et al. (2017).

The directions of strong emission in the two velocity ranges are slightly correlated, such that locations of strong emission from the DIG near 45 km s^{-1} mostly have strong emission near 100 km s^{-1} as well. The correlation is more significant towards the W43 region, whereas it is weak near $\ell \sim 24°$ as shown in Figure 7. This may suggest that the two velocity ranges towards W43 represent flows of interacting ionized gas (see §3.1.3), whereas the two velocity ranges towards the $\ell \sim 24°$ region could be caused by DIG emission at two distinct distances.

3.3. H I and the Diffuse Gas

It is uncertain whether a substantial amount of cold H I gas can coexist with the diffuse ionized gas in regions

with strong RRL emission from the DIG. If the radiation field in such regions is strong enough to ionize a large fraction of the gas, we may be able to observe a depletion in H I at locations and velocities of strong DIG emission (Miller & Cox 1993; Domgoergen & Mathis 1994).

This relationship has been probed by Zurita et al. (2002) who find that the H I distribution does not correlate (or anti-correlate) at all with the diffuse Hα emission tracing the ionized gas in the face-on galaxy NGC 157. The angular resolution of their H I map, however, does not match the better resolution of their Hα map. As a result, they would not be able to resolve H I depletion cavities much smaller than 1 kpc. A previous study by Reynolds et al. (1995) analyzed the same correlation for Hα-emitting H I clouds in the Milky Way. They find that the neutral and ionized components in these clouds are likely spatially separated. Since they
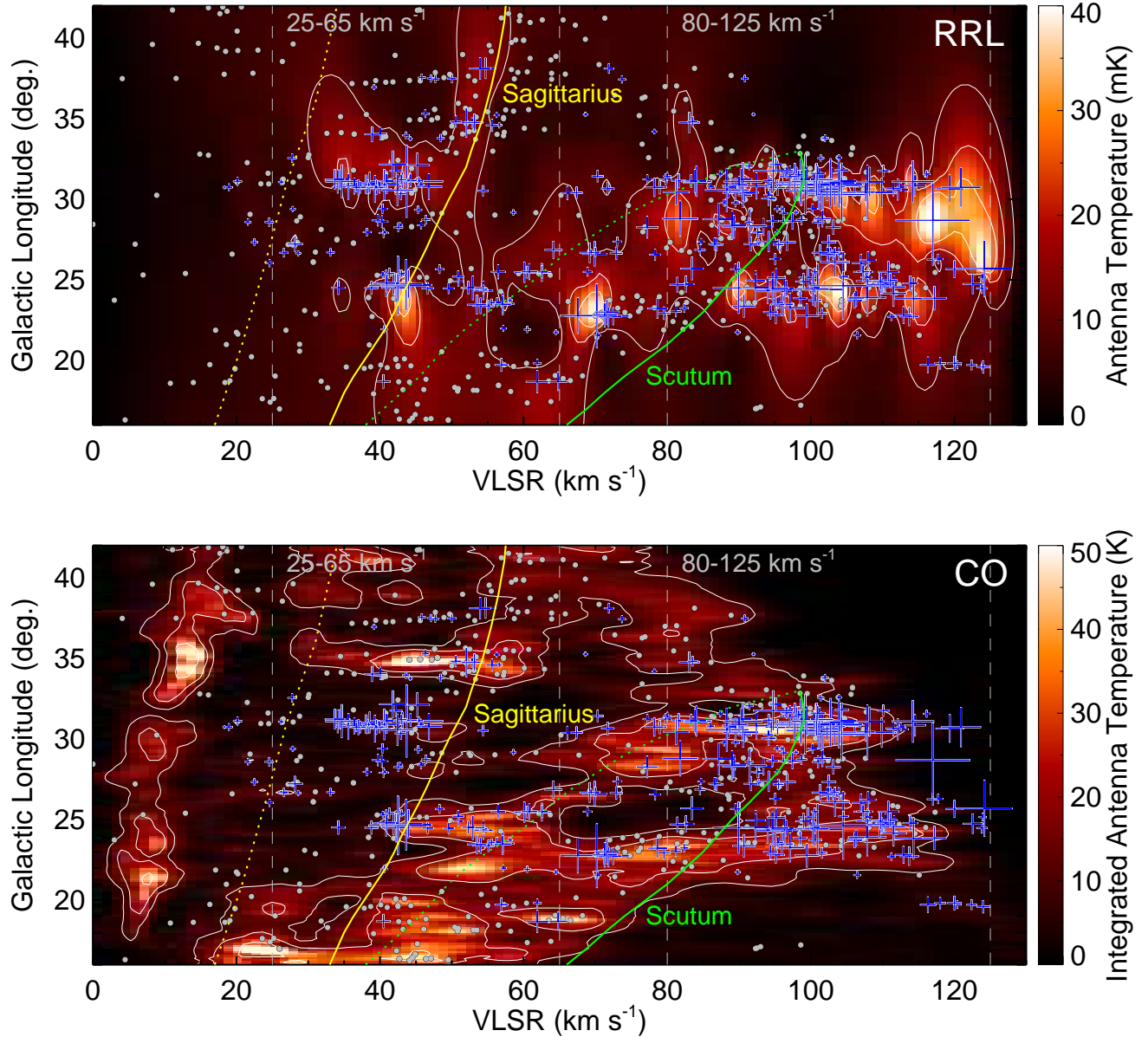
Figure 5. Top: Longitude-velocity diagram of the DIG. The white contours are at 10, 20, and 30 mK. The blue crosses denote the directions at which RRL spectra were taken and the cross sizes are proportional to the fitted H RRL intensities. The gray dots indicate discrete H II regions. The Sagittarius and Scutum spiral arms are traced in yellow and green, respectively (data from Reid et al. 2016). The dashed vertical lines indicate the two dominant velocity ranges: the 45 km s^{-1} component at 25-65 km s^{-1} and the 100 km s^{-1} component at 80-125 km s^{-1}. Bottom: Same, for Galactic ^{12}CO emission, integrated in the range from $-1°$ to $+1°$ in latitude (see Dame et al. 1987). Contours are at 10, 20, and 40 K.

only observed a relatively small region of the sky away from the Galactic plane, their available sample size is limited.

We use the VGPS H I data to test whether regions with strong emission from the DIG show a deficiency in H I. The VGPS data cubes have a spatial resolution of $1' \times 1'$ and a spectral resolution of 1.56 km s^{-1}. For the W43 region near $\ell \sim 31°$ we find an apparent H I

depletion cavity at 92 km s^{-1} (Figure 8, top left panel) which is consistent with our strong DIG emission shown in Figure 4. We find a similar depletion cavity for the $\ell \sim 23°$ region at 60 km s^{-1} (see Figure 8, top right panel) which is, however, offset by $\sim1.5°$ from the strong DIG emission seen in the 45 km s^{-1} component near $\ell \sim$ 24.5° (Figure 4). Our large number of RRL pointings near the $\ell \sim 24°$ region makes it unlikely that this offset

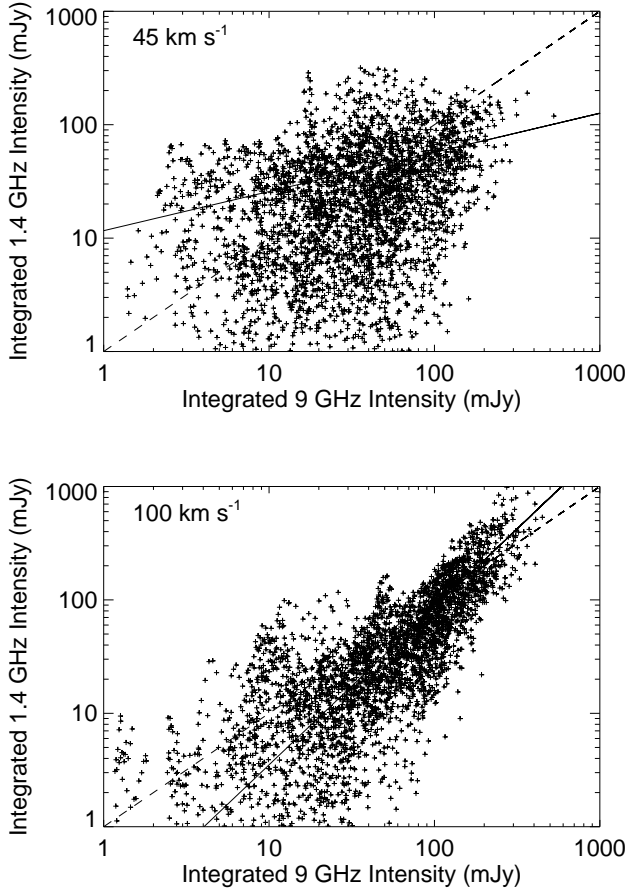**Figure 6.** Top: Correlation of the diffuse gas emission between our interpolated data at 9 GHz and the 1.4 GHz map from Alves et al. (2015) for the 45 km s^{-1} velocity component. We assume a GBT gain of 2 K Jy^{-1} and integrate the intensity over a pixel size of 36 sq. arcmin for both data sets. The solid line is a power-law fit of the form $y = ax^b$, with $a = 11.6321 \pm 0.0295$ and $b = 0.3452 \pm 0.0006$. The dashed line is a 1:1 relation. Bottom: Same, for the 100 km s^{-1} velocity component. The power-law fit parameters are $a = 0.1440 \pm 0.0003$ and $b = 1.3874 \pm 0.0004$.

is an artifact from our interpolation algorithm. We did not find any other strong H I depletion cavities in the velocity ranges of significant emission from the DIG for the sky zones in Figure 8.

Comparison of our RRL data with ^{13}CO maps casts doubt on whether strong ionized gas emission is usually spatially associated with a deficiency in H I. Using ^{13}CO GRS data, we can determine for both our regions whether these deficiencies are caused by H I self-absorption or due to an actual lack of H I gas. H I self-absorption, first described in detail by Knapp (1974), is usually correlated with CO emission features (Burton et al. 1978; Garwood & Dickey 1989). We find substantial ^{13}CO emission at the two directions and ve-
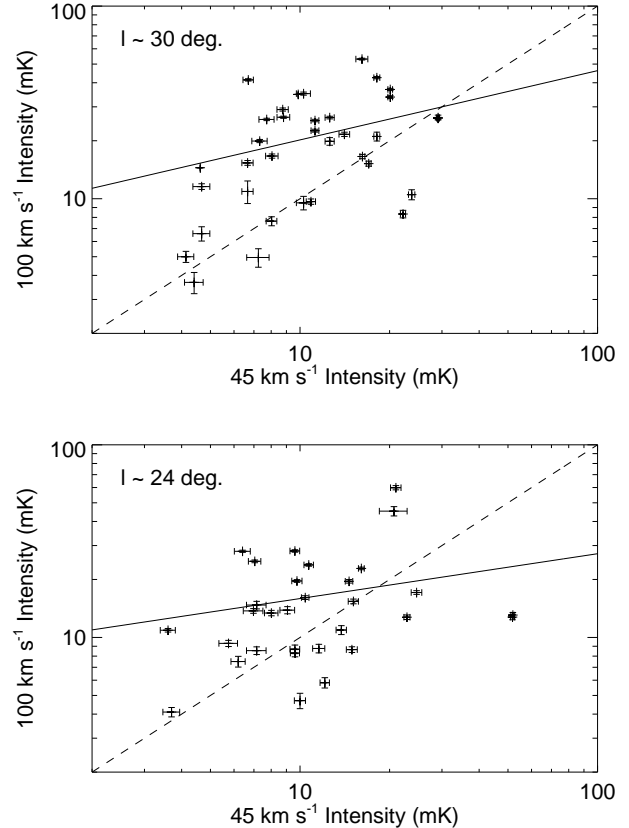
Figure 7. Top: Correlation between the observed 45 km s^{-1} and 100 km s^{-1} DIG intensities towards W43 ($\ell \sim 30°$). Each data point corresponds to a location where the RRL spectrum shows two hydrogen line profiles: one with a LSR velocity in the 25–65 km s^{-1} range (the 45 km s^{-1} component), and one with a LSR velocity in the 80–125 km s^{-1} range (the 100 km s^{-1} component). Error bars are $\pm 1\sigma$. The solid line is a power-law fit of the form $y = ax^b$, with $a = 8.8281 \pm 0.3453$ and $b = 0.3595 \pm 0.0149$. The R^2 of the regression is 0.141. The dashed line is a 1:1 relation. Bottom: Same, for the $\ell \sim 24°$ region. Here, $a = 9.3157 \pm 0.4008$ and $b = 0.2327 \pm 0.0160$ (R^2 = 0.058).

locities (Figure 8, bottom panels). In fact, the integrated ^{13}CO emission found at $\ell \sim 31°$ and $\ell \sim 23°$ is among the strongest within the range of the GRS. This suggests that the lack in H I emission is caused by H I self-absorption and is not due to an actual deficiency in H I gas.

3.4. *Correlation with 8.0 μm Intensity*

Emission from polycyclic aromatic hydrocarbons (PAHs) within the 8.0 μm band is usually caused by softer ultra-violet (UV) radiation than that responsible for RRL emission from H II regions. For example, Robitaille et al. (2012) show, using radiative transfer models, that most of PAH heating is provided by B
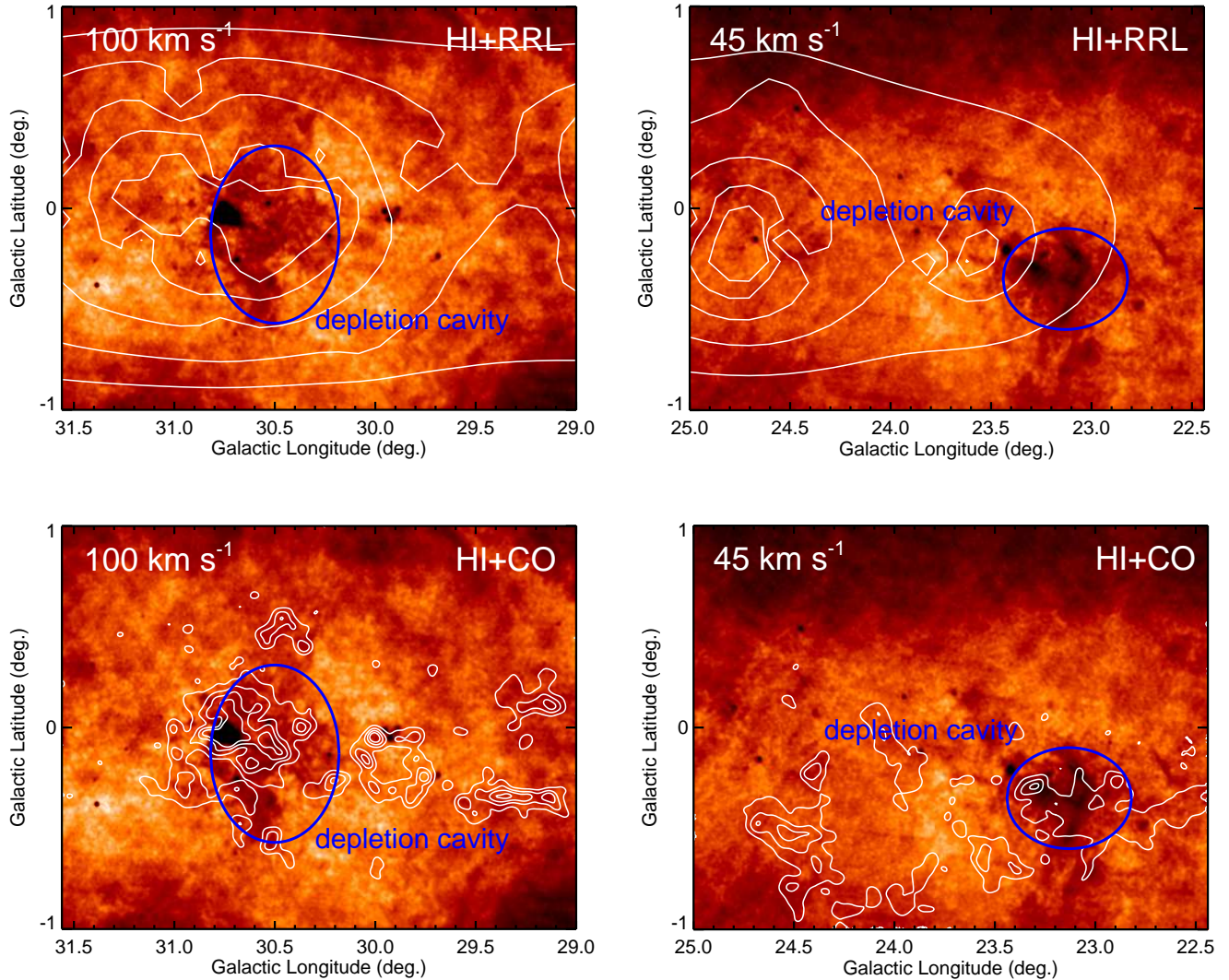
Figure 8. Comparison of RRL emission from the DIG with H I and CO emission reveals that deficiencies in H I emission are more likely due to self-absorption rather than gas displacement by the DIG. Top left: The VGPS H I map at 92 km s^{-1} for the $29° < \ell < 31.5°$ region, linearly scaled from 0 to 150 K brightness temperature. The white contours show our interpolated diffuse gas map at the 100 km s^{-1} velocity component at 4, 8, 12, 16, and 20 mK. A deficiency in H I emission is clearly visible at $\ell \sim 30.5°$, the location of W43. Top right: VGPS H I map at 60 km s^{-1} for the $22.5° < \ell < 25°$ region, with contours of our 45 km s^{-1} diffuse gas map and same increments as above. An H I deficiency is visible at $\ell \sim 23°$ which is, however, not spatially correlated with the diffuse gas emission. Bottom left: Same as top left, but with blue GRS ^{13}CO contours at the same velocity. Contours are at 0.5, 1, 1.5, and 2 K antenna temperature. The CO emission is spatially correlated with the H I bubble above, indicating that the deficiency in H I emission may be caused by H I self-absorption. Bottom right: Same, for the $22.5° < \ell < 25°$ region at 60 km s^{-1}.

stars, compared to RRL emission typically caused by O stars. While the 8.0 μm emission is often associated with strong PDRs surrounding discrete H II regions, there exists significant PAH emission that originates from the diffuse gas without nearby H II regions. Below, we analyze this "diffuse" PAH emission and its relation to the DIG. In the bottom panel of Figure 9 we show a map of the point-source subtracted 8.0 μm *Spitzer* GLIMPSE

emission (Benjamin et al. 2003; Churchwell et al. 2009). Since there is also strong 8.0 μm emission from discrete H II regions, we blank out these regions based on their corresponding positions and sizes from the WISE catalog, Version 1.4 (Anderson et al. 2014). In the upper panel of Figure 9 we show histograms of the location of single-velocity and multiple-velocity H II regions.
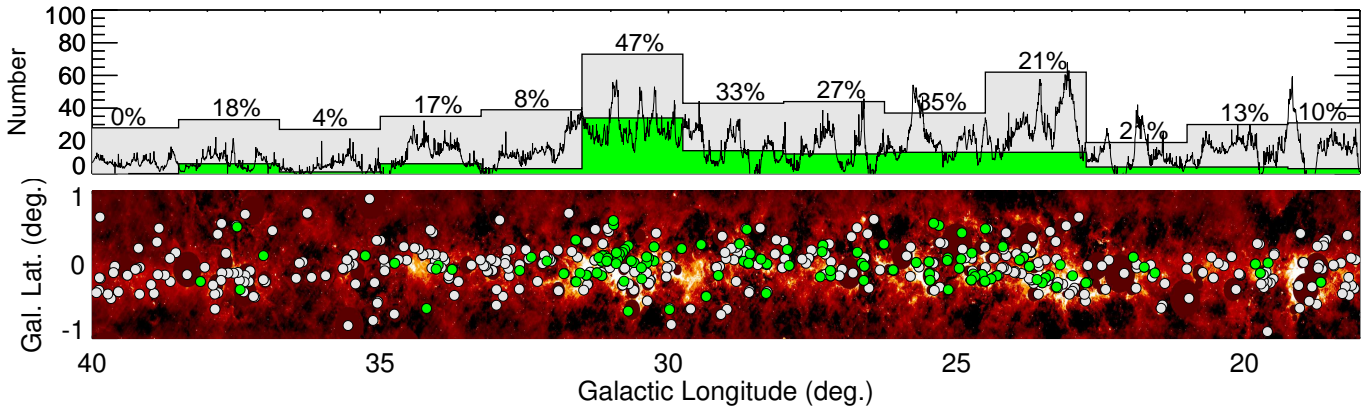
Figure 9. Locations of multiple-velocity H II regions. In the bottom panel, the background image is the point-source subtracted 8.0 μm *Spitzer* GLIMPSE emission, on a square-root scale ranging from -5 to 50 MJy sr⁻¹. Multiple-velocity H II regions are shown in green and single velocity H II regions are shown in gray. Emission around H II regions is blanked out according to their positions and sizes from the WISE catalog (Anderson et al. 2014). In the top panel we show histograms of the number of single-velocity H II regions (gray) and multiple-velocity H II regions (green). The numbers above the histogram indicate the percentage of multiple-velocity regions over the given longitude range. The black curve in the top panel shows the 8.0 μm GLIMPSE emission from the bottom panel integrated over all latitudes. There is a correlation between the number of H II regions and the 8.0 μm intensity (see Figure 10).

We observe a correlation between the location of discrete H II regions and the intensity of the 8.0 μm emission (see Figure 10). Both of these diffuse emission components should be caused by UV photons leaking from the discrete H II regions. The PAHs responsible for the 8.0 μm emission are destroyed in the hard UV radiation within an H II region (Voit 1992; Povich et al. 2007), but can survive where the radiation field is softer, i.e. in the diffuse ISM. The correlation therefore suggests that either a significant amount of the (soft) UV photons responsible for the 8 μm emission is leaking from the discrete H II regions or that the harder UV radiation produced by the O stars softens as it escapes into the ISM. Such a radiation softening has been suggested by Reynolds & Tufte (1995) and was recently observed indirectly for the compact H II region NGC 7538 (Luisi et al. 2016).

We also observe a correlation between the hard UV radiation field within the DIG and the softer UV radiation field responsible for PAH emission. Our method probes the radiation field strengths by using the observed RRL emission from the DIG and the 8.0 μm emission intensities as a proxy for the diffuse hard UV and soft UV radiation field strengths, respectively. A correlation between the intensities of these two emission components indirectly tests for a correlation between the radiation fields. We determine the diffuse 8.0 μm background by integrating the 8.0 μm flux in a circular 41″ aperture centered at each of the 135 off-target directions. By only using the off-target directions, we ensure that we are only sampling the diffuse 8.0 μm background, and not the emission associated with H II region PDRs. We then

compute the fluxes using our Kang software[3]. Kang is an astronomical visualization and analysis package written in IDL. Its relevant functionality here is that it can compute aperture photometry measurements using arbitrary aperture shapes.

We compare the diffuse 8.0 μm emission with the integrated intensity from all hydrogen RRLs at all velocities detected at an off-target direction. We plot in Figure 11 the correlation between the diffuse 8.0 μm emission and the integrated RRL intensity. Figure 11 indicates that the hard UV radiation is correlated with the softer UV radiation, as one would expect, although there is quite a large scatter.

Furthermore, the correlation appears to change above 35 mK. This may be due to the destruction of the PAH molecules that are largely responsible for the diffuse 8.0 μm emission. A similar effect has been observed by Lebouteiller et al. (2011) in the Galactic H II region NGC 3603. Direct PAH destruction typically requires photons with energies >20 eV which exist in sufficient numbers only in the most energetic radiation fields (e.g., within H II regions). The binding energy of H atoms to PAHs, however, is only ∼4.8 eV (Voit 1992). Thus, even less energetic radiation fields can contribute to PAH dissociation. The relatively strong hydrogen ionizing radiation field (≥ 13.6 eV) within regions with substantial RRL emission from the DIG must therefore partly be responsible for PAH dissociation. Considering that this effect limits the abundance of PAHs in these regions,
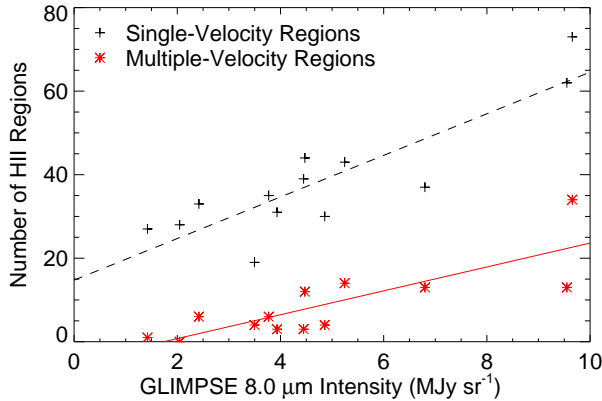
---

[3] http://www.bu.edu/iar/files/script-files/research/kang/

Figure 10. Correlation between $8.0\,\mu m$ emission from PAHs and the number of H II regions. Each data point represents one histogram bin from Figure 9, averaged over the entire $|b| < 1°$ latitude range. The dashed line is a linear fit of the form $y = a + bx$ for the single-velocity regions, with $a = 14.743 \pm 0.6056$ and $b = 4.9803 \pm 0.1127$. The solid line is the fit for the multiple-velocity regions, with $a = -4.9657 \pm 0.6057$ and $b = 2.8588 \pm 0.1127$. The correlation indicates that a significant amount of soft UV radiation is present near discrete H II regions.
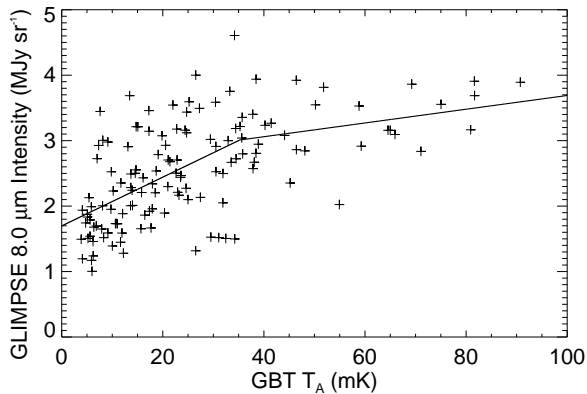

Figure 11. Correlation between $8.0\,\mu m$ emission from PAHs and RRL emission from the DIG. The RRL emission is from our pointed GBT observations of the diffuse gas. We average the point-source subtracted $8.0\,\mu m$ *Spitzer* GLIMPSE intensity over a $41''$ radius aperture (the beam size of the RRL observations) at the directions of our GBT observations. The two straight lines show linear fits, and indicate that the intensity of the far-UV radiation responsible for the RRL emission is correlated with the softer UV radiation responsible for the $8.0\,\mu m$ emission. The break between the fits is at GBT $T_A = 35\,\text{mK}$ which suggests that above this temperature PAHs are destroyed in highly energetic radiation fields, leading to a saturation in IR emission.

it comes as no surprise that we observe a saturation in PAH emission.

Clearly, further study of this correlation is required. Most helpful would be additional pointings toward cleaner sight lines where the source of the UV photons can be more easily be determined. A more direct measurement of the radiation field strength is difficult. Recently, Stock & Peeters (2017) described a technique to estimate the UV field intensity using the ratio between two PAH spectral components at $7.6\,\mu m$ and $7.8\,\mu m$. While this technique has not yet been applied to the diffuse ISM, it may prove useful in constraining properties of the radiation field outside H II regions.

4. SUMMARY

Here, we analyze the DIG using hydrogen RRL emission line spectra in the range $\ell = 18°$ to $40°$ which are either devoid of H II region emission or have multiple velocity components. Our data set is comprised of 353 RRL emission line components from the DIG. These allow us to determine the intensity and distribution of the diffuse gas.

We find that the DIG is spatially concentrated in two areas near $\ell = 31°$ and $\ell = 24°$, with two dominant velocity components ($45\,\text{km s}^{-1}$ and $100\,\text{km s}^{-1}$) in each of the areas. We investigate the KDA for the two velocity ranges and conclude that the $100\,\text{km s}^{-1}$ component has a Galactocentric distance of $\sim 6\,\text{kpc}$, corresponding to the location of W43. This suggests that much of the $100\,\text{km s}^{-1}$ gas is associated with W43. The origin of the $45\,\text{km s}^{-1}$ component is less clear. The intensity of the emission in the two velocity ranges is slightly correlated near $\ell = 31°$, which may imply that both velocity components originate at a single distance. In this case, the $45\,\text{km s}^{-1}$ component may arise from complex streaming motions near the end of the Galactic bar. For the $\ell = 24°$ region, however, it is unlikely that the observed velocity components are due to this effect. As an alternative, we suggest that the $45\,\text{km s}^{-1}$ emission may have its origin at a Galactocentric distance of $\sim 12\,\text{kpc}$, or a combination of both. Unfortunately, our current data are insufficient to clearly distinguish between these cases, a problem which may be investigated in future work. Future work may also explore in more detail the connection between the DIG observed in RRL emission, the more diffuse component observed in Hα, and the different environments these data are tracing.

Since regions with strong RRL emission from the DIG may show a deficiency in H I, we examine data from the VGPS for H I depletion cavities. We find such a bubble in H I emission for the W43 region at $\ell \sim 31°$ at $92\,\text{km s}^{-1}$. We also find a second bubble at $\ell \sim 23°$ and $60\,\text{km s}^{-1}$ which is, however, offset by $\sim 1.5°$ from the direction of strong DIG emission at $\ell \sim 24.5°$. There is strong ^{13}CO emission associated with these locations, suggesting that the deficiency in H I emission is rather

caused by H I self-absorption than an actual lack of H I gas.

The intensity of the RRL emission from the DIG is also correlated with the intensity of diffuse *Spitzer* GLIMPSE $8.0\,\mu$m emission, implying that the soft UV photons responsible for creating the infrared emission have a similar origin as the harder UV photons required for the RRL emission. The diffuse $8.0\,\mu$m emission appears to saturate at locations with the strongest RRL emission suggesting that the PAHs responsible for the $8.0\,\mu$m emission are destroyed by the radiation field in these regions.

Facility: Green Bank Telescope.

Software: TMBIDL (Bania et al. 2014), Kang.

REFERENCES

Alves, M. I. R., Calabretta, M., Davies, R. D., et al. 2015, MNRAS, 450, 2025

Alves, M. I. R., Davies, R. D., Dickinson, C., et al. 2012, MNRAS, 422, 2429

—. 2010, MNRAS, 405, 1654

Anderson, L. D. 2010, PhD thesis, Boston University

Anderson, L. D., Bania, T. M., Balser, D. S., et al. 2014, ApJS, 212, 1

Anderson, L. D., Bania, T. M., Balser, D. S., & Rood, R. T. 2011, ApJS, 194, 32

Anderson, L. D., Bania, T. M., Balser, D. S., & Rood, R. T. 2012, ApJ, 754, 62

Anderson, L. D., Hough, L. A., Wenger, T. V., Bania, T. M., & Balser, D. S. 2015, ApJ, 810, 42

Anderson, L. D., Deharveng, L., Zavagno, A., et al. 2015, ApJ, 800, 101

Balser, D. S., Rood, R. T., Bania, T. M., & Anderson, L. D. 2011, ApJ, 738, 27

Bania, T., Wenger, T., Balser, D., & Anderson, L. 2014, tmbidl: TMBIDL v7.1, Zenodo, 10.5281/zenodo.32790, ,

Bania, T. M., Anderson, L. D., & Balser, D. S. 2012, ApJ, 759, 96

Bania, T. M., Anderson, L. D., Balser, D. S., & Rood, R. T. 2010, ApJL, 718, L106

Benjamin, R. A., Churchwell, E., Babler, B. L., et al. 2003, PASP, 115, 953

Beuther, H., Meidt, S., Schinnerer, E., Paladino, R., & Leroy, A. 2017, A&A, 597, A85

Beuther, H., Tackenberg, J., Linz, H., et al. 2012, A&A, 538, A11

Binney, J., & Tremaine, S. 2008, Galactic Dynamics: Second Edition (Princeton University Press)

Bissantz, N., & Gerhard, O. 2002, MNRAS, 330, 591

Burton, W. B., Liszt, H. S., & Baker, P. L. 1978, ApJL, 219, L67

Churchwell, E., Babler, B. L., Meade, M. R., et al. 2009, PASP, 121, 213

Dame, T. M., Ungerechts, H., Cohen, R. S., et al. 1987, ApJ, 322, 706

Domgoergen, H., & Mathis, J. S. 1994, ApJ, 428, 647

Ferguson, A. M. N., Wyse, R. F. G., Gallagher, III, J. S., & Hunter, D. A. 1996, AJ, 111, 2265

Garwood, R. W., & Dickey, J. M. 1989, ApJ, 338, 841

Haffner, L. M., Reynolds, R. J., & Tufte, S. L. 1999, ApJ, 523, 223

Haffner, L. M., Dettmar, R.-J., Beckman, J. E., et al. 2009, Reviews of Modern Physics, 81, 969

Hoyle, F., & Ellis, G. R. A. 1963, Australian Journal of Physics, 16, 1

Knapp, G. R. 1974, AJ, 79, 527

Kolpak, M. A., Jackson, J. M., Bania, T. M., Clemens, D. P., & Dickey, J. M. 2003, ApJ, 582, 756

Kuchar, T. A., & Bania, T. M. 1994, ApJ, 436, 117

Langer, W. D., Velusamy, T., Goldsmith, P. F., et al. 2017, ArXiv e-prints, 1708.02310

Lebouteiller, V., Bernard-Salas, J., Whelan, D. G., et al. 2011, ApJ, 728, 45

Liu, B., McIntyre, T., Terzian, Y., et al. 2013, AJ, 146, 80

Luisi, M., Anderson, L. D., Balser, D. S., Bania, T. M., & Wenger, T. V. 2016, ApJ, 824, 125

Miller, III, W. W., & Cox, D. P. 1993, ApJL, 417, 579

Murray, N., & Rahman, M. 2010, ApJ, 709, 424

Nguyen Luong, Q., Motte, F., Schuller, F., et al. 2011, A&A, 529, A41

Povich, M. S., Stone, J. M., Churchwell, E., et al. 2007, ApJ, 660, 346

Reid, M. J., Dame, T. M., Menten, K. M., & Brunthaler, A. 2016, ApJ, 823, 77

Reid, M. J., Menten, K. M., Brunthaler, A., et al. 2014, ApJ, 783, 130

Renaud, F., Bournaud, F., Emsellem, E., et al. 2013, MNRAS, 436, 1836

—. 2015, MNRAS, 454, 3299

Reynolds, R. J. 1984, ApJ, 282, 191

Reynolds, R. J., Hausen, N. R., Tufte, S. L., & Haffner, L. M. 1998, ApJL, 494, L99

Reynolds, R. J., & Tufte, S. L. 1995, ApJL, 439, L17

Reynolds, R. J., Tufte, S. L., Kung, D. T., McCullough, P. R., & Heiles, C. 1995, ApJ, 448, 715

Robitaille, T. P., Churchwell, E., Benjamin, R. A., et al. 2012, A&A, 545, A39

Roman-Duval, J., Jackson, J. M., Heyer, M., et al. 2009, ApJ, 699, 1153

Roshi, D. A., & Anantharamaiah, K. R. 2001, ApJ, 557, 226

Rubin, R. H. 1968, ApJ, 154, 391

Sellwood, J. A., & Sánchez, R. Z. 2010, MNRAS, 404, 1733

Stil, J. M., Taylor, A. R., Dickey, J. M., et al. 2006, AJ, 132, 1158

Stock, D. J., & Peeters, E. 2017, ApJ, 837, 129

Voit, G. M. 1992, MNRAS, 258, 841

Zhang, B., Moscadelli, L., Sato, M., et al. 2014, ApJ, 781, 89

Zurita, A., Beckman, J. E., Rozas, M., & Ryder, S. 2002, A&A, 386, 801

Zurita, A., Rozas, M., & Beckman, J. E. 2000, A&A, 363, 9